International Journal of Greenhouse Gas Control 111 (2021) 103475

Contents lists available at ScienceDirect

International Journal of Greenhouse Gas Control

journal homepage: www.elsevier.com/locate/ijggc

Pore scale modeling and evaluation of clogging behavior of salt crystal aggregates in CO_2-rich phase during carbon storage

Mohammad Masoudi [a,*], Hossein Fazeli [a,c], Rohaldin Miri [b], Helge Hellevang [a]

[a] Department of Geosciences, University of Oslo, Pb. 1047, Blindern, Oslo 0316, Norway
[b] Department of Chemical, Petroleum and Gas Engineering, Iran University of Science and Technology, Narmak, Tehran 16846, Iran
[c] Institute of GeoEnergy Engineering, Heriot-Watt University, Edinburgh EH14 4AS, UK

ARTICLE INFO

Keywords:
Probabilistic nucleation
Lattice Boltzmann method
CO_2 Storage
Salt aggregation
Clogging model
Salt self-enhancing
Reactive transport modeling
Mineral precipitation
Nucleation and growth
Porosity-permeability relations

ABSTRACT

The optimal CO_2 storage operation requires high permeability in the near-well region in order to keep it safe and cost-efficient. Nucleation and growth of salt crystals driven by the evaporation of formation water into under-saturated (dry) super-critical CO_2 streams result in the changes in porosity and permeability of the near well-bore area. Permeability reduction is one of the main reasons for injectivity losses in the context of CO_2 storage in saline aquifers. According to recent studies, during CO_2 storage, salt crystals grow in two different forms: 1) single, large crystals in the aqueous phase, and 2) aggregates of micro-meter size salt crystals in the CO_2-rich vapor phase. All previous numerical studies at pore-scale have addressed the formation of single, large crystals in the aqueous phase. In this work we have developed a 3D pore-scale reactive transport solver based on a D3Q19 advection-diffusion Lattice-Boltzmann model. The model takes for the first time salt nucleation into consideration via a new probabilistic approach to simulate the formation of micro-meter size salt crystal aggregates in the CO_2-rich phase and their effect on changes in pore morphology and permeability. Comparing the results of porosity-permeability relations with some of the well-known clogging models, confirms the need for a new clogging model to capture the permeability reduction caused by salt aggregates.

1. Introduction

Carbon capture and storage (CCS) is a relatively new technology where CO_2 is captured from major point sources before it reaches to the atmosphere and is safely stored in underground geological reservoirs (geological storage). Deep saline aquifers are the most promising option for CO_2 storage to mitigate climate change. Deep saline aquifers have huge storage capacities, usually from ~2,000 to 20,000 Gt CO_2 (Bachu and Adams, 2003). Nevertheless, the annual emission of greenhouse gases related to worldwide energy consumption is also large (~ 33 Gt CO_2 in 2018) and as time goes on, the world demand for energy increases, and so does the emission of the greenhouse gasses. Therefore, the need for reduction is imminent and CCS is a key technology to avoid energy and climate crisis at the same time. This means that CO_2 sequestration will not accomplish major climate change mitigation unless it is executed on a very large scale with high injection rates. In order to achieve and maintain high injection rates in deep saline aquifers, one needs to have a detailed assessment of well injectivity and the process that can alter near-well permeability and results in injectivity decline. To maximize safety and cost-efficiency of CO_2 storage, it is necessary to understand how a high permeability in the near-well region is maintained.

1.1. Salt precipitation

Injection of large amounts of dry (under-saturated), supercritical CO_2 into saline aquifers leads to evaporation of formation water into the CO_2 stream and concentration build-up of dissolved salt in the aqueous phase. When salt concentration in the formation water goes beyond its solubility limit under the given thermodynamic state, the excess salt will precipitate out of the aqueous phase and immediately alter the porosity and permeability of the reservoir (Miri et al., 2015; Miri and Hellevang, 2016). Several field (Baumann et al., 2014; Grude et al., 2014; Talman et al., 2020), experimental (Berntsen et al., 2019; Kim et al., 2013; Miri et al., 2015; Nooraiepour et al., 2018), and numerical studies (Parvin et al., 2020; Zeidouni et al., 2009) have provided evidences for salt precipitation during CO_2 storage.

Salt crystals form in two different forms (Miri et al., 2015):

* Corresponding author.
E-mail address: mohammad.masoudi@geo.uio.no (M. Masoudi).

https://doi.org/10.1016/j.ijggc.2021.103475
Received 7 May 2021; Received in revised form 15 September 2021; Accepted 22 September 2021
Available online 4 October 2021

1) single, large crystals in the aqueous phase
2) aggregates of micrometer sized crystals in the CO_2-rich vapour phase

Single, large crystals form when the crystals are in contact with low- to moderately supersaturated solution and have enough time to grow. The aggregates of small crystals form near the interface in the CO_2 stream where the supersaturation and driving force for nucleation is large. The newly formed salt crystals are strongly water wet and can imbibe the fresh brine to the CO_2 stream. Evaporation of water from the fresh brine results in new nucleation and formation of new salt crystals on the previous small crystals. Repetition of these processes over and over leads to formation of salt aggregates that form a porous structure with massive capillarity. This phenomena is called "salt self-enhancing growth" and can lead to massive salt aggregates (Miri et al., 2015).

However there are several numerical works on the salt precipitation pattern, the salt self-enhancing growth has been overlooked in almost all of them. For instance, Dashtian et al. (2018) has developed a pore-network model to study the effects of pore size correlation on salt precipitation patterns because of evaporation in porous media. Their model takes capillary effects, vapour diffusion, brine flow, and salt transport into consideration. However, they stated that it is not possible to consider the saltself-enhancing growth into a pore-network model because this phenomenon occurs at the molecular scale and referred to their molecular dynamic simulation (Dashtian et al., 2017) for modelling this process.

A recently conducted study on the Aquistore CO_2 storage site, which is a part of SaskPower's Boundary Dam CCS demonstration project, have revealed the formation of salt crystals inside the injection well (Talman et al., 2020). They have stated that salt self-enhancing growth might be the reason behind the water backflow and salt formation inside the injection well (Talman et al., 2020). Such results highlights the importance of taking both forms of salt crystal into consideration. Both forms of the crystals can change the morphology of the porous structure and reduce the permeability, CO_2 transmissibility, and injectivity. As a result, it is necessary to take into account both forms of salt crystals in order to have a proper and robust porosity-permeability relation or a clogging model in the context of CO_2 storage.

1.2. Clogging models

Pore-scale modelling provides the possibility of simulating volume changes in different reactive transport phenomena after certain sub-grid geometric assumptions. The permeability of an altered pore space can also be calculated directly by computing the flow parameters, such as velocity vectors, with solving mass and momentum conservation equations (continuity and Navier-Stokes equations). In contrast, permeability is one of the input parameters for solving the flow equation (continuity equation coupled with Darcy equation) in continuum-scale modelling (Ertekin et al., 2001). Because every parameter has an average value on the continuum scale, one must deal with permeability changes using only available parameters. Porosity is the only parameter that is directly related to the changes in pore volume. The changes in porosity can be easily determined from the volume of deposited solids. In the other words, porosity-permeability relations (clogging models) are the tools for upscaling the changes in pore morphology at pore-scale to continuum-scale.

Several phenomena can alter the porosity and permeability of a porous medium such as mineral precipitation and dissolution, wax and asphaltene deposition, fatigue, swelling and shrinking, mineral cementation, biomass accumulation, and so forth. Different processes alter the porous structure in their own specific way and identical changes in porosity might lead to completely different changes in permeability depending strongly on the process causing the changes, the host environment and materials, and the mechanism behind the changes. Therefore, it is of great importance to use different porosity-permeability relations for upscaling different processes.

This work focuses on salt precipitation during CO_2 storage. In the context of CO_2 storage, the extent of modelled formation damage and injectivity alteration is controlled by the chosen clogging model irrespective of mechanisms occurring at pore scale. Parvin et al. (2020) have done a sensitivity analysis on four well-known clogging models and showed that the clogging models are a major source of uncertainty in modelling of CO_2 storage. Different clogging models can result in huge differences in permeability for the same amount of porosity reduction.

Most of the clogging models have been developed based on the homogeneous layer of salt covering grain surfaces. The most popular relation in this context is the Verma and Pruess model (Verma and Pruess, 1988), where a porous medium is conceptualized as a series of connected tubes of varying sizes. Put differently, all of the proposed clogging models are only applicable to the large, single crystals growing in the aqueous phase and might not be able to capture clogging caused by salt aggregates in the gas phase at a capillary or diffusive regime, and clogging models for micrometer size salt aggregates should be addressed separately. In this work, we developed a 3D pore-scale reactive transport model based on a D3Q19 advection-diffusion Lattice-Boltzmann model to simulate the formation of salt aggregates and their effect on changes in pore morphology and permeability. We then evaluated if any of the most used clogging models are able to capture the permeability reduction caused by salt aggregates and proposed a new approach for including salt aggregates into the clogging models in this context. In order for our model to be able to capture the formation of salt aggregates, we had to take the nucleation process into account.

1.3. Probabilistic mineral nucleation

Nucleation is the first step of any precipitation process forming new minerals. The position of the nucleation of the secondary minerals in the pore space and the way that the formed minerals grow in porous media have major effects on the porosity-permeability relation. Therefore, an understanding of the spatial distribution of stable secondary nuclei is crucial for a precise prediction of the hydrodynamics of porous media after mineral precipitation. Despite this, few reactive transport models have taken into account the nucleation process and in their models, nucleation occurs when concentration reaches a certain threshold value (Chen et al., 2014, 2012). However, as suggested by Hellevang et al., after a combination of numerical and experimental study on spatial distribution of secondary mineral growth along a basalt column, nucleation is a probabilistic process (Hellevang et al., 2019). They explained the formation of few and large crystals at random locations by overall control by a nucleation process and suggested that in order to get the distribution of secondary crystals in the numerical models, a new probabilistic approach must be developed for the nucleation phenomenon. This led to the development of a new probabilistic nucleation model in which the induction time is considered as a random variable (Fazeli et al., 2020; Nooraiepour et al., 2021). The random induction time statistically spreads around the measured or reported induction time, which can be either obtained from experiments or approximated by the classical exponential nucleation rate equation suggested by the classical nucleation theory (CNT). In this work, we used classical nucleation theory. In our model, both location and time of nucleation is probabilistic which can have a major effect on transport properties in different time and length scales.

We implemented the new probabilistic model into the 3D pore-scale Lattice Boltzmann (LB)-based reactive transport model in order to simulate the formation of salt aggregates.

2. Model description

The detailed explanation of the probabilistic nucleation model can be found in (Fazeli et al., 2020; Nooraiepour et al., 2021). In the following, we will explain the Lattice Boltzmann model for advection-diffusion-reaction and hydrodynamics. The main references

for Lattice Boltzmann models are our previous works (Fazeli et al., 2020, 2019, 2018) and Krüger et al. (2017).

2.1. LB model for advection-diffusion-reaction

We used Lattice Boltzmann method to solve the advection-diffusion-reaction (ADR) equation for tracking the concentration of salt in the solution:

$$\frac{\partial C_j}{\partial t} + \nabla.(uC_j) = \nabla.(D_j \nabla C_j) + R_j \tag{1}$$

Where C_j [NL^{-3}] is the aqueous concentration of species j, D_j [L^2T^{-1}] is diffusion coefficient of species j in water, u is velocity [LT^{-1}], and R_j [$NL^{-3}T^{-1}$] is the source/sink term due to reactions for species j. The discretized LB equation used to solve the ADR equation (the mass transport) is as follows:

$$g_i^j(x + c_i\Delta t, t + \Delta t) = g_i^j(x,t) - \frac{\Delta t}{\tau_g}\left(g_i^j(x,t) - g_i^{eq,j}(x,t)\right) + \Delta t Q_i^j(x,t) \tag{2}$$

$$g_i^{eq,j} = w_i C^j \left(1 + \frac{c_i.u}{c_s^2}\right) \tag{3}$$

In which g_i^j is discrete distribution function, $g_i^{eq,j}$ is equilibrium distribution function, Q_i^j is source/sink term, and C^j is concentration of species j. Δt is time resolutions, τ_g is advection-diffusion relaxation time, c_s is lattice speed of sound, and c_i and w_i are discrete velocity sets and weighting coefficients. For the D3Q19 lattice scheme (Fig. A.1), where 3 is the number of spatial dimensions (x, y, and z) and 19 is the number of discrete velocities, w_0=1/3, $w_{1\text{-}6}$=1/18, and $w_{7\text{-}18}$=1/36 and

$$c_i = \begin{cases} (0,0,0), & i = 0 \\ (\pm 1,0,0),(0,\pm 1,0),(0,0,\pm 1), & i = 1-6 \\ (\pm 1,\pm 1,0),(\pm 1,0,\pm 1),(0,\pm 1,\pm 1) & i = 7-18 \end{cases} \tag{4}$$

After solving the Eq. (2), the concentration of species j is calculated using the following relation:

$$C^j = \sum_i g_i^j \tag{5}$$

The source and sink term is given by

$$Q_i^j(x,t) = w_i\left(q_N^j(x,t) + q_G^j(x,t) + q_E^j(x,t)\right) \tag{6}$$

$$q_N^j = \frac{dC_N^j}{\Delta t} \tag{7}$$

$$q_G^j = \frac{dC_G^j}{\Delta t} \tag{8}$$

Subscribes N, G, and E in Eq. (6) are related to nucleation, growth, and evaporation of the solution on top of the domain, respectively. dC_N^j is concentration difference caused by the nucleation events. It is calculated by counting the number of nuclei formed at each time step. A nucleus is assumed to be a sphere of 10 nm radius. dC_G^j is concentration difference caused by crystal growth. dC_N^j and dC_G^j have negative values because mineral nucleation and growth cause mass loss from the solution. Put differently, q_N^j and q_G^j are sink terms and q_E^j is a source term.

According to Chapman-Enskog analysis, the following relation should exist between diffusion coefficient and the relaxation parameter in order for Eq. 2 to recover the advection-diffusion-reaction equation (Eq. 1):

$$D = c_s^2\left(\tau_g - \frac{\Delta t}{2}\right) \tag{9}$$

2.2. LB model for hydrodynamics

In order to recover the hydrodynamic properties in single-phase fluid flow, continuity equation (Eq. 10) and Navier-Stokes equation (Eq. 11) should be solved simultaneously. To do so, we used the LB model in Eq. 12.

$$\nabla.u = 0 \tag{10}$$

$$\rho\frac{\partial u}{\partial t} + \rho u.\nabla u = -\nabla P + \mu\nabla^2 u + F \tag{11}$$

where ρ [ML^{-3}] is density, u [LT^{-1}] is velocity, P [$M^1L^{-1}T^{-2}$] is pressure, μ [$M^1L^{-1}T^{-1}$] is dynamic viscosity and F [$M^1L^{-2}T^{-2}$] is body force.

$$f_i(x + c_i\Delta t, t + \Delta t) = f_i(x,t) - \frac{\Delta t}{\tau}\left(f_i(x,t) - f_i^{eq}(x,t)\right) + \left(1 - \frac{\Delta t}{2\tau}\right)F_i(x,t) \tag{12}$$

$$f_i^{eq} = w_i\rho\left(1 + \frac{u.c_i}{c_s^2} + \frac{(u.c_i)^2}{2c_s^4} - \frac{u.u}{2c_s^2}\right) \tag{13}$$

$$F_i = w_i\left(\frac{c_i.F_\alpha}{c_s^2}\right) \tag{14}$$

$$c_s^2 = \frac{1}{3}\left(\frac{\Delta x}{\Delta t}\right)^2 \tag{15}$$

where Δt and Δx are time and space resolutions. f_i is discrete distribution function, f_i^{eq} is equilibrium distribution function for hydrodynamics. F_i is body force, c_s is lattice speed of sound, u is velocity, ρ is density, and τ is relaxation time for hydrodynamics. It should be noted that the lattice speed of sound, c_s, can vary based on the chosen lattice structure. Because we used the same lattice structure (D3Q19), weighting coefficients (w_i), and discrete velocity sets (c_i) for ADR LB and hydrodynamics LB, the lattice speed of sound in Eq. 15 can be used for both Eq. 3 and Eq. 13. After solving Eq. 12, density and velocity can be calculated from the following equations:

$$\rho = \sum_{i=0}^{18} f_i^j \tag{16}$$

$$u = \frac{1}{\rho}\sum_i f_i\, c_i + \frac{F_\alpha}{2\rho} \tag{17}$$

Like advection–diffusion LB, by doing Chapman−Enskog analysis on Eq. 12, it can be shown that the relation between kinematic viscosity, υ, and relaxation parameter should be fulfilled to LB model cover the Navier-Stokes equation:

$$\upsilon = c_s^2\left(\tau - \frac{\Delta t}{2}\right) \tag{18}$$

We used the LB model for hydrodynamics to calculate horizontal permeability of the domain before and after salt aggregation. We used Darcy's law to calculate the permeability of the porous media:

$$\overline{J} = -\frac{k}{\mu}\nabla P \tag{19}$$

Where $\overline{J}$[LT^{-1}] is average flux (flow rate per unit area), k [L^2] is permeability, μ [$M^1L^{-1}T^{-1}$] is dynamic viscosity, and ∇P [$M^1L^{-1}T^{-2}$] is pressure gradient. ∇P in Eq. 19 can be replaced by F, the body force, in Eq. 11.

2.3. Numerical implementation

Fig. A.2 shows the flowchart of the LBM model for ADR. The followings are the explanation of the numerical implementations.

2.3.1. Evaporation

Continuous evaporation of water into the CO_2 stream results in the constant increase in salt concentration in the aqueous phase. When the

concentration of salt reaches its solubility limit, the extra salt precipitates out in the form of solid salt crystals. In order to mimic the evaporation process without dealing with a complex multiphase flow simulator, we designed the following simulations:

The simulation domain is 70 × 70 × 70 grids with the grid resolution of 10 μm. We generated a random porous structure with porosity around 30% using the PoreSpy open source code (Gostick et al., 2019). All the boundaries are no flux boundary. The domain is initially saturated with brine. In each time step, the solution becomes more concentrated at the first layer after the top boundary using the source term, $q_E^j(x,t)$ in Eq. (6). This can mimic the evaporation process as well as capillary suction when the salts start to precipitate and form porous aggregates. It can represent a block of porous media in the CO_2 stream; saturated with CO_2 and with a liquid film covering its grains. The water film becomes more concentrated as the water evaporates to the gas phase, resulting in the formation of salt aggregates. By continuously increasing the concentration of solution on top of the domain, the model can also mimic the imbibition of the brine by salt aggregates to the evaporation front.

2.3.2. Nucleation

The first step of the salt formation is nucleation. In this work, induction time varies statistically and is considered as a random variable in the probabilistic nucleation model. The probabilistic induction time (τ_P) is stochastically spread around the deterministic (measured or reported) induction time (τ_N). As it was explained earlier, in this work, the deterministic mean induction time, τ_N [nuclei^{-1}m^{2}s], is computed based on the classical nucleation theory (CNT):

$$\ln(\tau_N) = \frac{\widehat{\Gamma}\sigma^3}{T^3(\ln(\Omega))^2} - \ln(k_N) \tag{20}$$

where T [K] is absolute temperature, Ω is saturation ratio providing the thermodynamic driving force for nucleation, σ [Jm^{-2}] is interfacial free energy between the nucleating phase and the substrate, and k_N [nucleim^{-2}s^{-1}] is nucleation rate constant. $\widehat{\Gamma}$ is a lumped parameter expressed as:

$$\widehat{\Gamma} = \beta v^2 K_B{}^{-3} \tag{21}$$

where β is a geometry factor, v [m^3/molecule] is the molecular volume of the nucleating phase, and k_B is the Boltzmann constant, 1.38×10^{-23} [JK^{-1}]. In Eq. (20), the values of σ and k_N need to be measured from laboratory experiments. More about the probabilistic nucleation and a sensitivity analysis on nucleation rate can be found in our previous work (Nooraiepour et al., 2021).

In the probabilistic nucleation model, the probability of forming a nucleus during a time step is expressed by a Gauss-Laplace (normal) probability density function (PDF). The following equations give the probability density function, P(x), and cumulative distribution function, F(x), of the Gaussian distribution:

$$P(x) = \frac{1}{sd\sqrt{2\pi}} e^{-\frac{(x-m)^2}{2sd^2}} 0 \le x \le 2\tau_N \tag{22}$$

$$F'(x) = P(x) \tag{23}$$

where, m is the mean ($m = \tau_N$), and sd is the standard deviation ($sd = \tau_N/4$) of the random variable x. To find probabilistic induction time (τ_p), a random number with probability (p) of $0 < p < 1$ is generated, then τ_p (between 0 and $2\tau_N$) is found such that the value of the normalized $F(x)$ at τ_p is equal to the p. Briefly, $F(x = \tau_p) = p$. Assigning a value to τ_p is iterated in each time step of the reactive transport simulation.

In Eq. 20, the induction time is defined for the unit of surface area, i.e., [nuclei^{-1}m^{2}s]. Therefore, in order for the induction time to be comparable to the elapsed time, the probabilistic induction time needs to be divided by the available surface area for nucleation, $\overline{\tau_p} = \tau_p / A_n$. It is assumed that one stable nucleus forms for each $\overline{\tau_p}$ that is longer than the period that the solution's saturation ratio remains unchanged or increased in contact with the substrate (the elapsed time). Therefore, if we call the random number generator N times to find $\overline{\tau_p}$ from F(x) until $\sum_N \overline{\tau_p} > \Delta t$, N-1 stable nuclei will form. Where, Δt is the elapsed time or the time interval during which nuclei counts are computed. After computing the number of stable nuclei, n, the concentration difference because of nucleation can be calculated as follows:

$$dC_{N,ph} = \frac{n\left(\frac{4}{3}\pi r_N^3\right)}{V_m V_{grid}} \tag{24}$$

Where subscript ph stands for the physical units, r_N [m] is the radius of a stable nucleus, V_m [m^{3}mol^{-1}] is the molar volume of the nucleating component, and V_{grid} [m^3] is the grid volume. $dC_{N,ph}$ should then be converted from physical units to LB units to obtain dC_N^j in Eq. 7. The number of precipitated crystals in each time step provides the reactive area provided for crystal growth. The reactive area is used as an input parameter for the growth rate computation. We refer the more interested readers to our previous work (Fazeli et al., 2020) for more details about the probabilistic nucleation model.

2.3.3. Salt aggregation

Taking the nucleation process into account, we prevent any homogeneous reaction in the bulk fluid. Put differently, salt precipitation only happens on the grains. As mentioned before, nucleation is a necessary condition for growth. In this work, in order to prevent further complexity, we consider the artificial single-species reaction, A(aq) ⇄ A (s). We control the necessary condition by the use of reactive surface area, S_r, in Eq. (25).

$$R = k S_r(1 - \Omega) \tag{25}$$

In Eq. (25), R [mols^{-1}] is the growth rate, k [molm^{-2}s^{-1}] is the growth rate constant, S_r [m^2] is reactive surface area, and Ω is saturation ratio:

$$\Omega = \frac{C_A}{C_{eq}} \tag{26}$$

Where, C_A [molL^{-1}] is the concentration of mineral A in the aqueous phase, corresponding to the ion activity product in classical thermodynamics, and C_{eq} [molL^{-1}] is the equilibrium aqueous concentration of mineral A corresponding to the equilibrium constant.

In ADR LB, the communication between the reaction and the transport is accomplished using an operator splitting method in a sequential non-iterative approach An et al., 2021; Fazeli et al., 2020, 2019, 2018; Patel, 2016; Steefel et al., 2015). This approach makes our model capable of being coupled with any geochemical solvers. When using an explicit coupling approach like the operator splitting method, one needs to ensure the time step is small enough to meet the Courant (for advection) and von Neumann (for diffusion) criteria; Eqs. (27) and ((28), respectively. If not, more than the entire content of one grid cell can be transferred to the next grid or mass could be transferred more than one grid cell in a single time step, resulting in operator splitting errors.

$$\frac{|\vec{u}|\Delta t}{\Delta x} \le 1 \tag{27}$$

$$\frac{D\Delta t}{\Delta x^2} \le 0.5 \tag{28}$$

Since we only have diffusion in our reactive transport problem, the von Neumann criterion should be satisfied. For τ_g=1 according to Eq. (9), $D\Delta t/\Delta x^2 \approx 0.167$. Therefore, the von Neumann criterion is automatically fulfilled in our model.

After each transport step, the code calls the reaction part to compute the source/sink term. Using a conversion factor, the concentration is

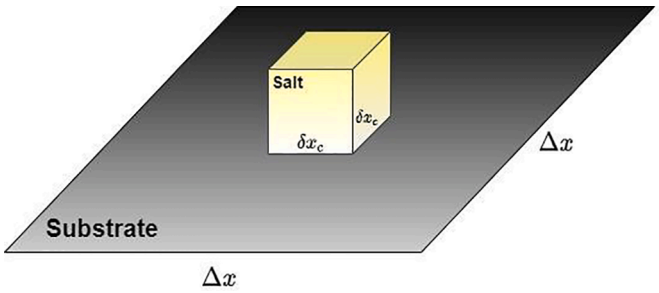

Fig. 1. Salt crystal growth at sub-grid scale.

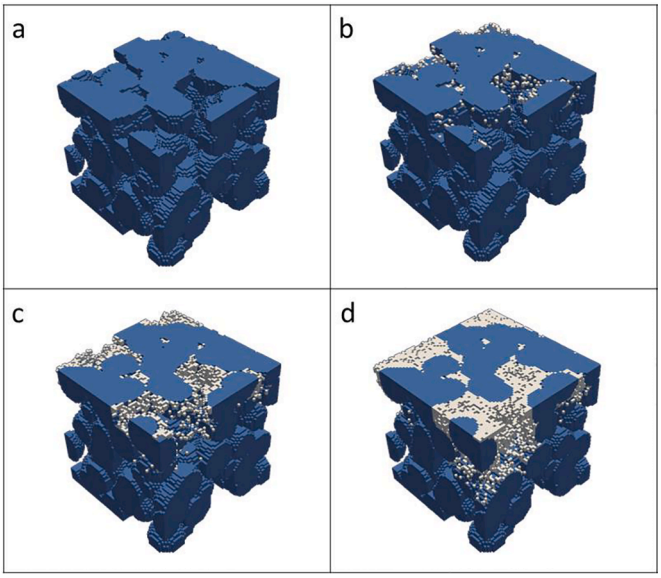

Fig. 2. Formation of salt aggregates at top of the simulation domain. Blues color represents the grains and with color represents the secondary mineral (salt aggregates) (a) at the beginning; (b) after 10000 time steps; (c) after 30000 time steps (d) after 100000 time steps.

first converted from LB unit to physical unit. The reactive surface area (S_r) is then updated and the reaction rate is calculated using Eq. (25). The concentration difference is then calculated as follows:

$$dC_{G,ph} = \frac{R\, dt_{ph}}{V_{grid}} \tag{29}$$

Where subscript *ph* stands for the physical units, dt_{ph} [s] is the physical timeframe of the reaction, and V_{grid} [m^3] is the volume of the grid. The final step is to convert the concentration difference from physical units to LB units for obtaining dC_R^j in Eq. 8. A thorough explanation of unit scales and conversion factors can be found in Krüger et al. (2017).

It should be noted that we used the same time step for reaction, nucleation, evaporation (sink/source term in Eq. (6)) and diffusion. This does not lead to concentration overshooting, since the physical time steps are small (0.02 s), as a consequence of fulfilling the von Neumann criterion and also because of the assumptions in geometry evolution (explained in the next section). However, to overcome the limitation of small time steps, one can use adaptive time stepping schemes such as PID (proportional, integral, differential), as described in (Patel, 2016). However, in this study, we did not focus on this aspect.

No nucleation and growth occur when saturation ratio is less than one ($\Omega<1$). As long as there is no nucleation in a grid, the reactive surface area is zero. When the first nucleation happens, it provides reactive surface area; a nucleus provides a surface area equivalent to a sphere of 10 nm radius. If the saturation ratio is more than one, the nuclei start to grow and use the excess dissolved salt for crystal growth until the solution reaches its solubility limit. When the solution reaches its solubility limit in a grid, the growth process stops and new nucleation is needed for more growth even if the saturation ratio is more than one. This approach allows us to simulate the formation of salt aggregates in the CO_2 phase.

2.3.4. Geometry evolution

We assume that a salt crystal grows in the middle of a grid as a cube (Fig. 1). The more the crystals grow, the more the reactive surface area is provided. In order to model the formation of salt aggregates, we considered three kinds of surfaces:

1- Primary surface: surface of the grains in the primary block of porous media (the darker colour in Fig. 2) which only provide surface area for nucleation.
2- Reactive secondary surface: precipitated salts, derived by either nucleation or growth, that have only been in contact with supersaturated solution ($\Omega>1$). These crystals provide surface area for both nucleation and growth.
3- Non-reactive secondary surface: precipitated salts, derived by either nucleation or growth, which have been in contact with the solution at its solubility limit ($\Omega\leq1$). These crystals only provide surface area for nucleation.

The molar amount of each type of precipitated salt is saved in each grid. Using the molar volume of salt and assuming that all the salts in a grid grow as a single cube at the middle of the grid, the provided surface area for reaction and nucleation can be calculated:

$$\delta x_r = 3\sqrt{n_r.V_m} \tag{30}$$

Where δx_r is the edge length of a cubic salt crystal, n_r is the molar amount of reactive salts in the grid, and V_m is the molar volume of the precipitated phase. If there are no fully-precipitated neighbour grids, the reactive surface area is calculated by Eq. (31.a) because as it is shown in Fig. 1, one side of the salt crystal is attached to the substrate.

$$S_r = 5(\delta x_r)^2 \tag{31.a}$$

A grid is considered as a solid-filled grid when the solid phase occupies more than 75% of its volume (Δx^3). However, when a grid is about to be fully-precipitated, the reaction rate is so high, mostly because of the large reactive surface area, that it usually ends up with filling more than the available volume. In this case, the extra amount of solid salt is equally divided between the available neighbors.

A fully-precipitated grid can provide reactive surface area for its neighbors as long as it does not contact with the solution at its solubility limit (where it becomes a non-reactive secondary surface). If there is a reactive surface area from neighbour grids, the average reactive surface area is calculated as follows:

$$S_r = 4(\delta x_r)^2 + S_{rn} \tag{31.b}$$

The subscript *rn* in Eq. (31.b) stands for *reactive neighbours*. Furthermore, the chance of nucleation on the secondary phase is higher than on the initial substrate(s) regardless of the type of the secondary phase; reactive or non-reactive. However, the non-reactive secondary surface does not contribute to reactions. The weighted arithmetic mean based on the surface area, Eq. (32), is used to calculate the average interfacial free energy, σ, used in Eq. (20), when we have different substrates in a grid cell. In this work, we assumed that the interfacial free energy between the nucleating phase and the initial substrate is 50 times larger than the interfacial free energy between the nucleating phase and the precipitated solids.

$$\overline{\sigma} = \frac{\sum_i S_i \sigma_i}{\sum_i S_i}, i = \text{type of substrates}, \tag{32}$$

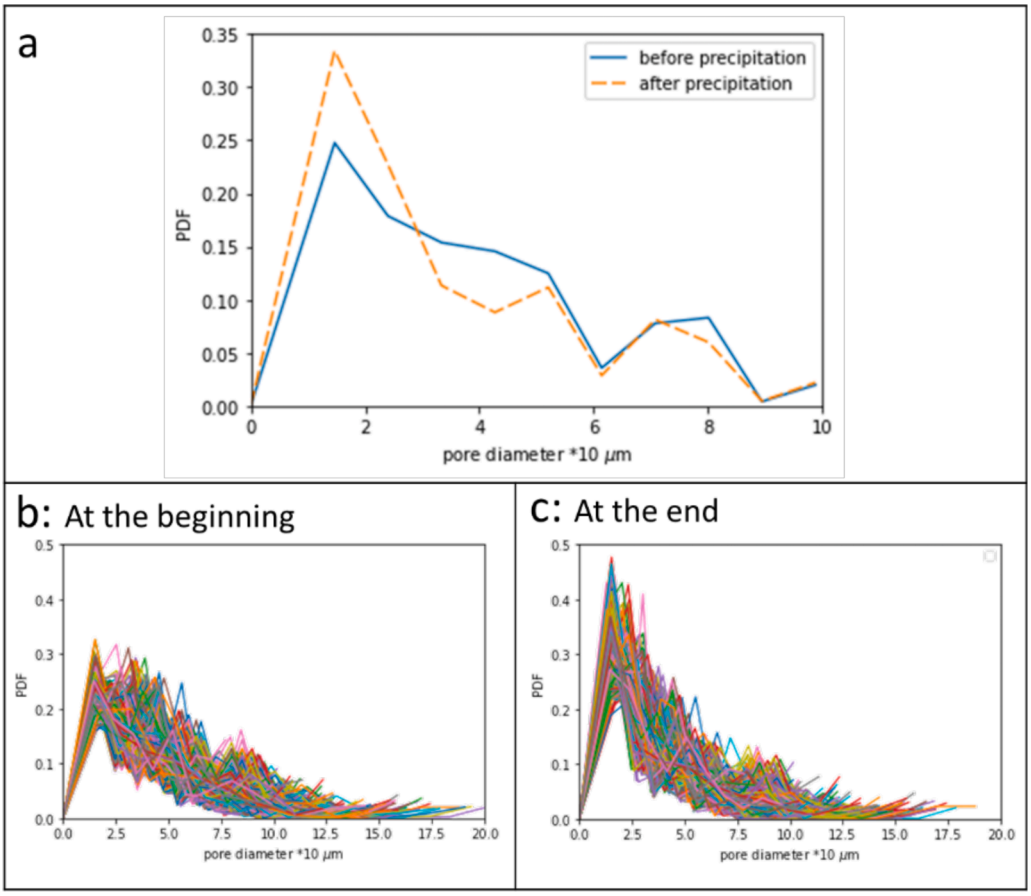

Fig. 3. Pore-size distribution of the simulation domains. a) The simulation domain shown in Fig. 2 before and after salt aggregation. b) Pore-size distribution of all the simulation domains at the beginning of the simulation. c) Pore-size distribution of all the simulation domains at the end of the simulation.

Table 1
Detailed information of the used clogging models.

Type	Formula	Reference	Parameters
Carman-Kozeny	$\frac{k}{k_0} = \left(\frac{\phi}{\phi_0}\right)^n \left(\frac{1-\phi_0}{1-\phi}\right)^2$	Zeidouni et al. (2009) (Tang et al., 2015)	n=3 n=2.4
Verma-Pruess	$\frac{k}{k_0} = \left(\frac{\phi/\phi_0 - \phi_r}{1-\phi_r}\right)^n$	(Verma and Pruess, 1988)	n=1 $\phi_r = 0.3$
		(Pruess and Müller, 2009)	n=2 $\phi_r = 0.9$
		(Giorgis et al., 2007)	n=4.1 $\phi_r = 0.3$
Power law	$\frac{k}{k_0} = \left(\frac{\phi}{\phi_0}\right)^n$		n=2 n=4

3. Results and discussions

We generated 800 random structures with porosity of around 30% using the PoreSpy open source code (Gostick et al., 2019). Fig. 2.a shows a sample of the simulation domains used in this study (the darker colour represents the grains). The simulation domain is initially saturated with a solution at its equilibrium concentration of salt (Ω=1). By increasing salt concentration near the top boundary, saturation ratio of the solution goes beyond unity and therefore, nucleation events might start to happen. The more the concentration, the higher the chance for nucleation. The simulation results showed that the developed model is able to simulate the formation of micrometer sized salt aggregates (Fig. 2). A full video of a simulation is provided in Appendix 2.

The key for the model to be able to simulate the formation of salt aggregates is the probabilistic nucleation model. When the first nuclei form, crystal growth starts. As it was explained in section 2.3.4, geometry evolution, more growth provides more reactive surface area and at the same time, more suitable substrates that promote more nucleation events and result in massive aggregation of salt crystals. As a result, as it is shown in Fig. 2.b, small salt crystals start to form on the grids near the top boundary of the simulation domain. The growth of salt crystal is a fast reaction that leads the solution towards the saturation ratio of one. When salts concentration reaches to its equilibrium aqueous concentration, the growth stops. More evaporation increases the saturation ratio repeatedly, resulting in new nucleation events and growth of new crystals. This process leads to formation of porous salt aggregates as it is shown in Fig. 2.c and d. The developed model can thereby mimic the "salt growth self-enhancement mechanism".

Fig. 3 shows the pore-size distribution of the simulation domains. Fig. 3.a depicts the pore-size distribution of the simulation domain shown in Fig. 2 at the beginning and the end of simulation (after 200,000 time steps). Fig. 3.b shows the pore-size distribution of all the simulation domains at the beginning of the simulation and Fig. 3.c shows the pore-size distribution of all the simulation domains at the end of the simulation. Because of the probabilistic nature of the model, each run leads to different results and structure.

As shown in Fig. 3.a, the number of smaller pores increases after massive salt aggregation on top of the domain. Additionally, a comparison between Fig. 3.b and Fig. 3.c clearly shows the increase in the number of small pores. Massive salt accumulation is observed in all the cases. The pore-size distribution curves are shifted to the left side. The increase in the number of small pores confirms the formation of micrometer size salt crystals. The smaller the pores, the higher the capillarity. Therefore, aggregation of small salt crystals forms a

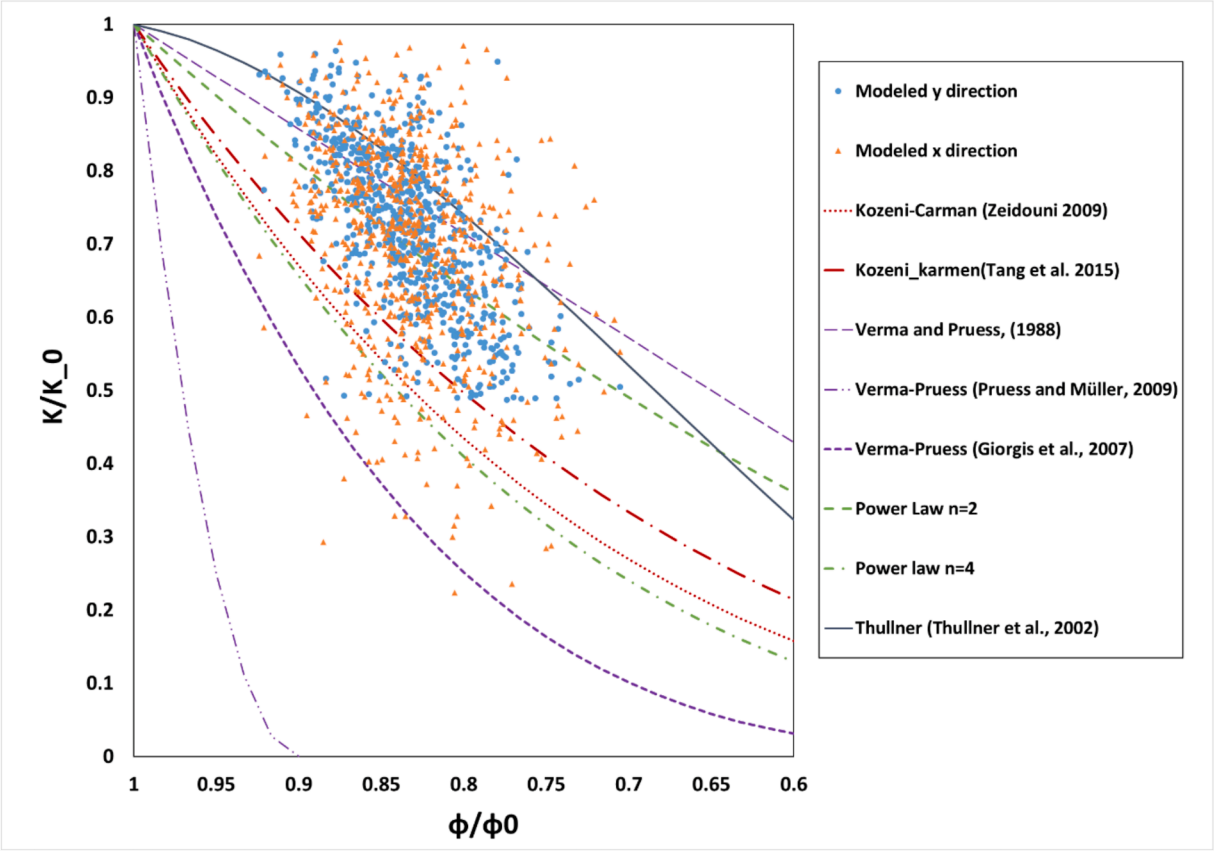

Fig. 4. Comparison of the results of the simulations with different clogging models.

secondary porous media with high capillarity.

As shown in Fig. 2 and Fig. 3, formation of salt aggregates changes pore architecture. Any modification in the structure of a porous medium can lead to change in hydrodynamic and transport properties of the porous medium. As we discussed earlier, the changes in the transport and flow properties at pore-scale can be directly modelled by solving different equations. (NS, ADE, ...) and determining local properties, such as velocity and concentration. At continuum scale, however, one needs to use up-scaling workflows and representative models to accommodate these changes and connect different time and length scales within a system. Porosity-permeability relations which usually referred to as clogging models are an upscaling technique to account for permeability evolutions due to changes in pore structure.

The question is if the most used clogging models are able to capture the permeability reduction caused by salt aggregates during CO_2 storage. To answer this question, we considered three widely used groups of clogging models in this context: 1) Carman-Kozeny relations, 2) Verma and Pruess relations, and 3) Power law relations as it is explained by Zhang and Liu (2016). The selected clogging models are the widely-used clogging models, which only rely on the parameters related to porosity and could be easily implemented into different simulators. We avoided more complex relations because they usually require more details that might not be available in all the cases, have a lot of tuning parameters, and their implementation often results in high computational costs. Furthermore, as it was pointed out by Hommel et al. (2018), there are no fundamental differences between the behaviour of power laws and more complex relations. The details of the used clogging models are presented in Table 1. We refer the interested readers to a review of existing porosity-permeability relations and their essential features by Hommel et al. (2018).

We computed horizontal permeability of the structures (in x and y directions) at the beginning and the end of simulations and compared the results with the clogging models reported in Table 1. The results are shown in Fig. 4. None of the clogging models can capture the relation between porosity and permeability properly. This is due to the physics behind these clogging models. The Carman-Kozeny model was originally developed to predict the permeability of a sphere packing. In the Verma and Pruess model, a porous medium is conceptualized as a series of connected tubes with different sizes and precipitation is assumed to happen on the walls of the tubes, reducing their radius. In other words, these models are likely to fail for modelling the behaviour of micrometer size salt aggregates in the CO_2 phase. However, they might be useful for single large salt crystals in the brine phase.

For developing a precise clogging model for carbon storage process, it is important to consider the fact that salt precipitation happens in two different forms (single large crystals in brine phase and micrometer size salt aggregates in gas phase) and both forms of the precipitation result in pore clogging and permeability reduction. However, the clogging happens in different ways. Such a behavior is also observed during biomass accumulation. Generally, biomass forms in two different ways of biofilms and aggregates in porous media. Aggregates have a variety of different shapes and develop distinct individual biomass colonies, which causes plugging. However, biofilms are continuous thin layers, which are uniformly distributed along the surface of a porous structure (Hommel et al., 2018).

Due to similarities of biomass colonies to the salt aggregates, we checked if the proposed clogging model by (Thullner et al., 2002) for biomass colonies can capture the clogging behaviour in our simulations:

$$\frac{k}{k_0} = a\left(\frac{\phi - \phi_{crit}}{\phi_0 - \phi_{crit}}\right)^3 + (1-a)\left(\frac{\phi - \phi_{crit}}{\phi_0 - \phi_{crit}}\right)^2 \tag{33}$$

Where a is a weighting factor and ϕ_{crit} is the critical porosity at which the permeability becomes zero. We used a=*-1.7* and $\phi_{crit} = 0.1$. As it is

shown in Fig. 4, this clogging model matches poorly with the results for the formation of salt aggregates. Thullner et al., (2002), Verma and Pruess (1988), and power law with n=2 give the best fits among the used clogging models with the R-squared (R^2) around 0.44.

However the model for biomass accumulations has the same performance as the power law model, the researches carried out in this context can provide insight into the challenges the researchers in CO_2 storage field may encounter in dealing with salt deposition during CCS operations. In models accounting for biomass accumulations, biofilm is the most commonly assumed form of growth. Vandevivere (1995) addressed this issue by breaking down the reduction mechanism into biofilms and aggregates and relating them with a weighting function. The same approach (two porosity-permeability relations) have been implemented in other works (Seki and Miyazaki, 2001; Thullner, 2010; Thullner et al., 2002) but our main inspiration came from Vandevivere relation (Vandevivere, 1995). We propose to split up the clogging mechanisms to single large crystals and salt aggregates and introduce the following equation:

$$\frac{k}{k_0} = S_g \underbrace{f_1\left(\frac{\phi}{\phi_0}\right)}_{\text{aggregate model}} + (1 - S_g) \underbrace{f_2\left(\frac{\phi}{\phi_0}\right)}_{\text{large crystal model}} \tag{34}$$

In Eq. (34), f_1 is related to salt aggregates, which form in CO_2 stream, and f_2 is related to large crystals, which form in the brine phase. Therefore, we can use gas or CO_2 saturation, S_g, as the weighting function in Eq. (34). Several works in the literature are about the single large crystals in the aqueous phase, such as the ones in Table 1. Obviously more studies are required in this context especially for validating the proposed relation. More works need to be done to develop a proper clogging model for salt aggregates (f_1). Additionally, more experimental data is needed to validate any proposed model and no experimental data is available at the time of developing this work. The main reason for the lack of experimental data is overlooking the fact that we deal with a relatively unlimited source of brine in an actual storage reservoir. This important part is completely overlooked in almost all of the experimental works in the context of salt deposition during CO_2 storage, especially core flood experiments. We have to content ourselves with this conceptual modelling approach and invite the researchers in this specific context to discuss possible solutions for addressing this issue and designing more representative experimental tests.

4. Conclusions

In this work, we developed a reactive transport LB model with a new probabilistic approach for nucleation. The specific numerical implementations of the nucleation and growth processes at sub-grid resolution provide the developed model the ability to simulate the formation of micrometer size salt aggregates during CO_2 storage in a saline aquifer for the first time. The analyses of the pore size distribution of 800 different structures show that the number of smaller pores increases after massive salt aggregation which confirms the formation of porous salt aggregates. Although because of the probabilistic nature of the nucleation model different structures have formed for different simulations, massive salt aggregation is found in all the cases.

We then checked if some of the widely-used clogging models can predict the amount of permeability reduction due to salt aggregates. The results showed that the used clogging models are not able to capture this kind of clogging. Based on the similarities of salt deposition and biomass accumulation, we proposed to split up the clogging mechanisms to single large crystals and salt aggregates. However, further studies (both experimental and numerical) are required to develop a proper clogging model for salt aggregates.

CRediT authorship contribution statement

Mohammad Masoudi: Conceptualization, Methodology, Software, Visualization, Writing – original draft, Software, Writing – review & editing. **Hossein Fazeli:** Software, Writing – review & editing. **Rohaldin Miri:** Conceptualization, Supervision, Writing – review & editing. **Helge Hellevang:** Conceptualization, Supervision, Writing – review & editing, Funding acquisition, Resources.

Declaration of Competing Interest

The authors declare that they have no known competing financial interests or personal relationships that could have appeared to influence the work reported in this paper.

Acknowledgments

This publication has been produced with support from the project "Preventing loss of near-well permeability in CO_2 injection wells (POREPAC), funded by the Research Council of Norway through the CLIMIT program (280651/E20), and from the NCCS Centre (257579/E20), performed under the Norwegian research program Centres for Environment-friendly Energy Research (FME). The authors acknowledge the following partners for their contributions: Aker Solutions, Ansaldo Energia, Baker Hughes, CoorsTek Membrane Sciences, EMGS, Equinor, Gassco, Krohne, Larvik Shipping, Lundin, Norcem, Norwegian Oil and Gas, Quad Geometrics, Total, and Vår Energi.

The computations were performed on the Norwegian Research and Education Cloud (NREC), using resources provided by the University of Bergen and the University of Oslo. http://www.nrec.no/.

Supplementary materials

Supplementary material associated with this article can be found, in the online version, at doi:10.1016/j.ijggc.2021.103475.

Appendix 1

Figs. A.1 and A.2.

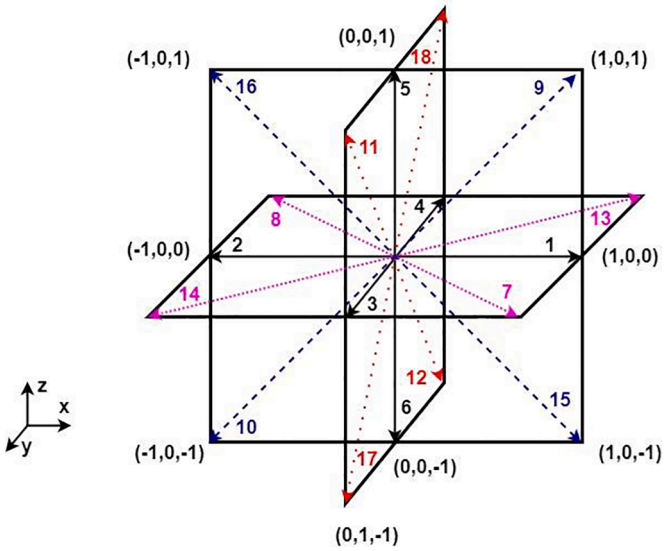

Fig. A.1. D3Q19 velocity sets. The length of the solid lines (velocity sets 1-6) is $|c_i| = 1.\Delta x$. The length of the dotted or dashed lines (velocity sets 7-19) is $|c_i| = \sqrt{2}.\Delta x$. C_0 is not shown.

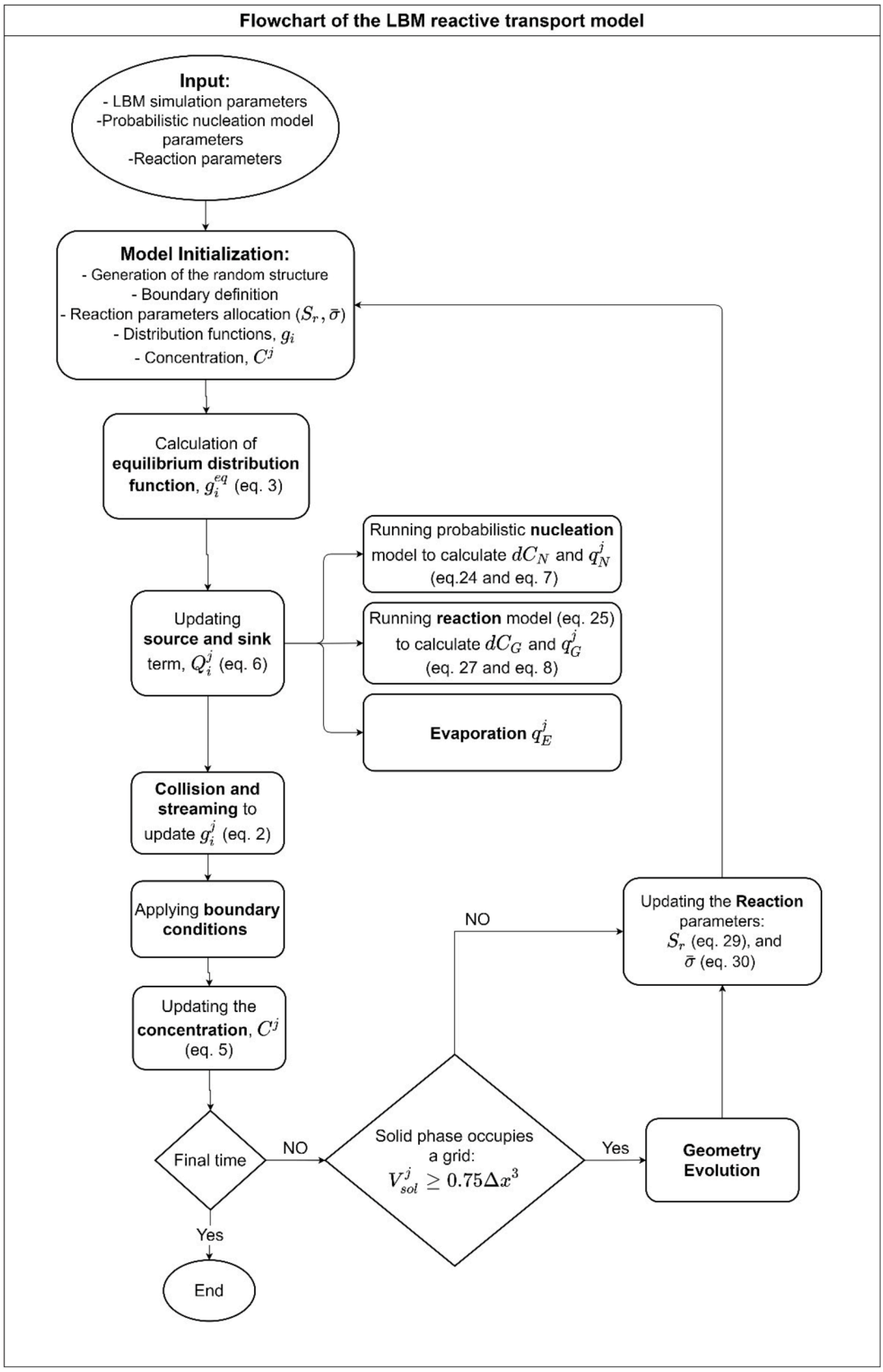

Fig. A.2. Flowchart of the LBM reactive transport model.

Appendix 2

A video of simulation of one case is provided.

References

An, S., Erfani, H., Hellevang, H., Niasar, V., 2021. Lattice-Boltzmann simulation of dissolution of carbonate rock during CO2-saturated brine injection. Chem. Eng. J. 408, 127235 https://doi.org/10.1016/j.cej.2020.127235.

Bachu, S., Adams, J.J., 2003. Sequestration of CO2 in geological media in response to climate change: capacity of deep saline aquifers to sequester CO2 in solution. Energy Convers. Manag. 44, 3151–3175.

Baumann, G., Henninges, J., De Lucia, M., 2014. Monitoring of saturation changes and salt precipitation during CO2 injection using pulsed neutron-gamma logging at the Ketzin pilot site. Int. J. Greenh. Gas Control 28, 134–146. https://doi.org/10.1016/j.ijggc.2014.06.023.

Berntsen, A., Todorovic, J., Raphaug, M., Torsæter, M., Chavez Panduro, E.A., Gawel, K., 2019. Salt clogging during supercritical CO2 injection into a downscaled borehole model. Int. J. Greenh. Gas Control 86, 201–210. https://doi.org/10.1016/j.ijggc.2019.04.009.

Chen, L., Kang, Q., Carey, B., Tao, W.-Q., 2014. Pore-scale study of diffusion–reaction processes involving dissolution and precipitation using the lattice Boltzmann method. Int. J. Heat Mass Transf. 75, 483–496. https://doi.org/10.1016/j.ijheatmasstransfer.2014.03.074.

Chen, L., Kang, Q., He, Y.-L., Tao, W.-Q., 2012. Mesoscopic Study of the Effects of Gel Concentration and Materials on the Formation of Precipitation Patterns. Langmuir 28, 11745–11754. https://doi.org/10.1021/la3020095.

Dashtian, H., Shokri, N., Sahimi, M., 2018. Pore-network model of evaporation-induced salt precipitation in porous media: the effect of correlations and heterogeneity. Adv. Water Resour. 112, 59–71. https://doi.org/10.1016/j.advwatres.2017.12.004.

Dashtian, H., Wang, H., Sahimi, M., 2017. Nucleation of salt crystals in clay minerals: molecular dynamics simulation. J. Phys. Chem. Lett. 8, 3166–3172.

Ertekin, T., Abou-Kassem, J.H., King, G.R., 2001. Basic applied reservoir simulation. Society of Petroleum Engineers, Richardson, TX.

Fazeli, H., Masoudi, M., Patel, R.A., Aagaard, P., Hellevang, H., 2020. Pore-Scale Modeling of Nucleation and Growth in Porous Media. ACS Earth Sp. Chem. 4, 249–260. https://doi.org/10.1021/acsearthspacechem.9b00290.

Fazeli, H., Patel, R., Hellevang, H., 2018. Effect of pore-scale mineral spatial heterogeneity on chemically induced alterations of fractured rock: a lattice Boltzmann study. Geofluids 6046182. https://doi.org/10.1155/2018/6046182, 2018.

Fazeli, H., Patel, R.A., Ellis, B.R., Hellevang, H., 2019. Three-dimensional pore-scale modeling of fracture evolution in heterogeneous carbonate caprock subjected to CO2-ENRICHED BRine. Environ. Sci. Technol. 53, 4630–4639. https://doi.org/10.1021/acs.est.8b05653.

Giorgis, T., Carpita, M., Battistelli, A., 2007. 2D modeling of salt precipitation during the injection of dry CO2 in a depleted gas reservoir. Energy Convers. Manag. 48, 1816–1826. https://doi.org/10.1016/j.enconman.2007.01.012.

Gostick, J.T., Khan, Z.A., Tranter, T.G., Kok, M.D.R., Agnaou, M., Sadeghi, M., Jervis, R., 2019. PoreSpy: a python toolkit for quantitative analysis of porous media images. J. Open Source Softw. 4, 1296.

Grude, S., Landrø, M., Dvorkin, J., 2014. Pressure effects caused by CO2 injection in the Tubåen Fm., the Snøhvit field. Int. J. Greenh. Gas Control 27, 178–187. https://doi.org/10.1016/J.IJGGC.2014.05.013.

Hellevang, H., Wolff-Boenisch, D., Nooraiepour, M., 2019. Kinetic control on the distribution of secondary precipitates during CO2-basalt interactions. In: E3S Web Conf., p. 98.

Hommel, J., Coltman, E., Class, H., 2018. Porosity–Permeability Relations for Evolving Pore Space: A Review with a Focus on (Bio-)geochemically Altered Porous Media. Transp. Porous Media 124, 589–629. https://doi.org/10.1007/s11242-018-1086-2.

Kim, M., Sell, A., Sinton, D., 2013. Aquifer-on-a-Chip: understanding pore-scale salt precipitation dynamics during CO2 sequestration. Lab Chip 13, 2508. https://doi.org/10.1039/c3lc00031a.

Krüger, T., Kusumaatmaja, H., Kuzmin, A., Shardt, O., Silva, G., Viggen, E.M., 2017. The lattice Boltzmann method, 10. Springer Int. Publ, pp. 4–15.

Miri, R., Hellevang, H., 2016. Salt precipitation during CO 2 storage-A review. Int. J. Greenh. Gas Control. https://doi.org/10.1016/j.ijggc.2016.05.015.

Miri, R., van Noort, R., Aagaard, P., Hellevang, H., 2015. New insights on the physics of salt precipitation during injection of CO2 into saline aquifers. Int. J. Greenh. Gas Control 43, 10–21. https://doi.org/10.1016/j.ijggc.2015.10.004.

Nooraiepour, M., Fazeli, H., Miri, R., Hellevang, H., 2018. Effect of CO 2 Phase States and Flow Rate on Salt Precipitation in Shale Caprocks - A Microfluidic Study. Environ. Sci. Technol. https://doi.org/10.1021/acs.est.8b00251.

Nooraiepour, M., Masoudi, M., Hellevang, H., 2021. Probabilistic nucleation governs time, amount, and location of mineral precipitation and geometry evolution in the porous medium. Sci. Rep. 11, 16397. https://doi.org/10.1038/s41598-021-95237-7.

Parvin, S., Masoudi, M., Sundal, A., Miri, R., 2020. Continuum scale modelling of salt precipitation in the context of CO2 storage in saline aquifers with MRST compositional. Int. J. Greenh. Gas Control 99, 103075. https://doi.org/10.1016/j.ijggc.2020.103075.

Patel, R.A., 2016. Lattice Boltzmann method based framework for simulating physico-chemical processes in heterogeneous porous media and its application to cement paste.

Pruess, K., Müller, N., 2009. Formation dry-out from CO2 injection into saline aquifers: 1. Effects of solids precipitation and their mitigation. Water Resour. Res. 45.

Seki, K., Miyazaki, T., 2001. A mathematical model for biological clogging of uniform porous media. Water Resour. Res. 37, 2995–2999. https://doi.org/10.1029/2001WR000395.

Steefel, C.I., Appelo, C.A.J., Arora, B., Jacques, D., Kalbacher, T., Kolditz, O., Lagneau, V., Lichtner, P.C., Mayer, K.U., Meeussen, J.C.L., Molins, S., Moulton, D., Shao, H., Šimůnek, J., Spycher, N., Yabusaki, S.B., Yeh, G.T., 2015. Reactive transport codes for subsurface environmental simulation. Comput. Geosci. 19, 445–478. https://doi.org/10.1007/s10596-014-9443-x.

Talman, S., Shokri, A.R., Chalaturnyk, R., Nickel, E., 2020. Salt precipitation at an active CO2 injection site. In: Gas Inject. into Geol. Form. Relat. Top. Wiley Online Books. https://doi.org/10.1002/9781119593324.ch11.

Tang, Y., Yang, R., Du, Z., Zeng, F., 2015. Experimental study of formation damage caused by complete water vaporization and salt precipitation in sandstone reservoirs. Transp. Porous Media 107, 205–218.

Thullner, M., 2010. Comparison of bioclogging effects in saturated porous media within one- and two-dimensional flow systems. Ecol. Eng. 36, 176–196. https://doi.org/10.1016/j.ecoleng.2008.12.037.

Thullner, M., Zeyer, J., Kinzelbach, W., 2002. Influence of microbial growth on hydraulic properties of pore networks. Transp. Porous Media 49, 99–122. https://doi.org/10.1023/A:1016030112089.

Vandevivere, P., 1995. Bacterial clogging of porous media: a new modelling approach. Biofouling 8, 281–291. https://doi.org/10.1080/08927019509378281.

Verma, A., Pruess, K., 1988. Thermohydrological conditions and silica redistribution near high-level nuclear wastes emplaced in saturated geological formations. J. Geophys. Res. https://doi.org/10.1029/JB093iB02p01159.

Zeidouni, M., Pooladi-Darvish, M., Keith, D., 2009. Analytical solution to evaluate salt precipitation during CO2 injection in saline aquifers. Int. J. Greenh. Gas Control 3, 600–611. https://doi.org/10.1016/J.IJGGC.2009.04.004.

Zhang, S., Liu, H.-H., 2016. Porosity–permeability relationships in modeling salt precipitation during CO2 sequestration: review of conceptual models and implementation in numerical simulations. Int. J. Greenh. Gas Control 52, 24–31. https://doi.org/10.1016/j.ijggc.2016.06.013.